



In situ anchoring in carbon matrix of $\text{Bi}_2\text{O}_2\text{CO}_3$ as a high-performance anode material for Li-ion batteries

Pu-Qiang He, Jun Guo*, Hui Huang*, Zhong-Cheng Guo

Received: 5 February 2024 / Revised: 5 March 2024 / Accepted: 7 March 2024 / Published online: 14 June 2024
© Youke Publishing Co., Ltd. 2024

Abstract Bismuth-based anode materials have been regarded as promising Li-ion batteries due to their high theoretical capacity. However, their low conductivity and associated volume expansion inhibited their commercialization. In this work, $\text{Bi}_2\text{O}_2\text{CO}_3$ @C composites were successfully synthesized by in situ anchoring of flower-like $\text{Bi}_2\text{O}_2\text{CO}_3$ nanosheets on a carbon-based substrate via hydrothermal. The unique composited structure of $\text{Bi}_2\text{O}_2\text{CO}_3$ @C leads to a stable specific capacity of $547 \text{ mAh}\cdot\text{g}^{-1}$ after 100 cycles at a current density of $0.1 \text{ A}\cdot\text{g}^{-1}$. Notably, it demonstrates excellent rate capability with a specific capacity of $210 \text{ mAh}\cdot\text{g}^{-1}$ at $5 \text{ A}\cdot\text{g}^{-1}$. After 550 cycles at a current density of $0.5 \text{ A}\cdot\text{g}^{-1}$, a high reversible capacity of nearly $400 \text{ mAh}\cdot\text{g}^{-1}$ was observed. Additionally, in situ X-ray diffraction measurements clearly demonstrate the conversion between Bi and Li_3Bi during alloying/dealloying, confirming the good electrochemical reversibility of the materials for Li storage. The reaction kinetics of

$\text{Bi}_2\text{O}_2\text{CO}_3$ @C were further investigated using galvanostatic intermittent titration technique. Furthermore, $\text{Bi}_2\text{O}_2\text{CO}_3$ @C exhibited excellent long-term stability, maintaining its high reversible capacity for over 200 cycles at a current density of $0.5 \text{ A}\cdot\text{g}^{-1}$ in a full cell configuration using $\text{Li}_{1.20}\text{Mn}_{0.54}\text{Ni}_{0.13}\text{Co}_{0.13}\text{O}_2$ as the cathode material. This result further underscores its promising potential for lithium-ion batteries. This work may provide inspiration for the design of alloy-type negative electrode materials for high-performance rechargeable batteries.

Keywords $\text{Bi}_2\text{O}_2\text{CO}_3$; Composite materials; Anode materials; Full batteries

1 Introduction

Li-ion batteries (LIBs) with merits of high energy density, operating voltage, compact size and environmentally friendliness have emerged as primary energy storage devices in various applications, such as electric vehicles, portable devices, smart grids and emerging electric transportation [1–7]. However, the current commercially available anode for LIBs remains graphite, which suffers from the low theoretical capacity ($372 \text{ mAh}\cdot\text{g}^{-1}$ for gravimetric capacity or $719 \text{ mAh}\cdot\text{cm}^{-3}$ for volumetric capacity) and inferior rate performance, rendering it insufficient to meet the high energy density requirements of LIBs [8–10]. To address the rapid growth in energy demand, it is imperative to design and develop LIBs with larger capacity, higher cycling stability and energy/power densities [11].

Alloy-based anode materials, such as Sb, Sn and Bi, have attracted considerable attention in terms of their ability to deliver high Li-ion-storage capacities [12–14]. Bi and its relevant composites, including Bi-based alloys,

Supplementary Information The online version contains supplementary material available at <https://doi.org/10.1007/s12598-024-02825-3>.

P.-Q. He, J. Guo*, H. Huang*, Z.-C. Guo
Faculty of Metallurgy and Energy Engineering, Kunming
University of Science and Technology, Kunming 650093, China
e-mail: 1038gj@kust.edu.cn; 1534279728@qq.com

H. Huang
e-mail: huihuanghan@kust.edu.cn

J. Guo, H. Huang, Z.-C. Guo
Research Center of Metallurgical Electrode Materials
Engineering Technology, Kunming 650106, China

H. Huang, Z.-C. Guo
Kunming Hendera Science and Technology Co., Ltd., Kunming
650106, China



have been regarded as promising candidates for the LIBs anode due to the high earth abundance, moderate operation voltage and special lamellar structure along *c*-axis [15–18]. The (003) interplanar spacing of Bi is 0.395 nm, which is beneficial to the alloying/dealloying reaction of alkaline metal ions during cycling procedure [16, 17, 19–21]. Even Bi anode possesses a not very high gravimetric capacity of 385 mAh·g⁻¹, but a high volumetric capacity of ~ 3800 mAh·cm⁻³ is under consideration due to the two-step intercalation process from Bi to LiBi and further to Li₃Bi, which enables the Bi anode to surpass its theoretical capacity [22, 23]. Nevertheless, alloy-semiconductor type anodes reveal the common problem of rapid capacity decay, deriving from the significant volume expansion/shrinkage during the discharge/charge procedure, leading to the pulverization of anode active materials and unstable solid electrolyte interface [24–26]. Therefore, strategies were used to mitigate the volume variation problem for alloy-semiconductor type anodes during discharge/charge process, including nanomaterials preparation [27, 28], microstructure design [3, 16, 29] and carbon composites [10, 17, 23, 27]. For instance, Xu et al. [30, 31] developed Bi nanoparticles and carbon framework composites that can efficiently regulate volume exchange and provide superior kinetics during the discharge/charge process. The rational design of structure and meticulous control of morphology in electrode active materials are widely acknowledged as effective strategies for significantly enhancing their electrochemical properties [32–34]. Therefore, the investigation of active materials with rational structure and morphology holds great potential for LIBs. Investigations have shown that electrode active materials, characterized by a three-dimensional heterostructure grown directly on conductive substrates, exhibit improved electrochemical performance [35]. This enhancement can be attributed to several factors, such as the increased active surface area, superior electron and charge transfer capabilities, enhanced structural integrity, and the beneficial synergistic effects between the matrix and active materials. Transition metal oxides/hydroxides have garnered considerable attention as potential electrode materials for LIBs [36–39]. Bi₂O₂CO₃, a Bi-based semiconductor material, has been widely used in the field of healthcare and plays a crucial role in the purification of air and wastewater treatment through photocatalysis [40, 41]. Additionally, nanosheets of Bi₂O₂CO₃ have shown advantageous properties as negative electrode active materials for supercapacitors [42]. However, to the best of our knowledge, there is limited literature available on the in situ growth of flower-like Bi₂O₂CO₃ nanosheets on carbon substrates as negative electrode active materials for Li-ion battery systems.

Beneficial from the aforementioned structural hybrid engineering, in this work, a composite material of flower-like Bi₂O₂CO₃ nanosheets in situ grown on a carbon-based substrate has been synthesized, which significantly improves the storage performance of Li⁺ by carefully adjusting the structure of the Bi₂O₂CO₃ nanosheets. The presence of a carbon-based substrate and graphene effectively mitigates the stress and strain caused by volume expansion. The Bi₂O₂CO₃ anode, with its distinctive structural advantages, demonstrates exceptional discharge capability of 547 mAh·g⁻¹ after 100 cycles at 0.1 A·g⁻¹. In situ X-ray diffraction (XRD) reveals that the Li storage mechanism of the Bi₂O₂CO₃@C anode undergoes an irreversible conversion reaction, followed by a reversible alloying reaction. To further evaluate the application potential of the Bi₂O₂CO₃@C anode, a full cell structure was established using Li_{1.20}Mn_{0.54}Ni_{0.13}Co_{0.13}O₂ (LMLC) as the cathode material. The assembled Bi₂O₂CO₃@C // LMLC full cell exhibits a reversible capacity of 174.1 mAh·g⁻¹ at 0.1 A·g⁻¹.

2 Experimental

2.1 Materials

Bismuth nitrate pentahydrate, sodium alginate (SA), ethylene glycol, thiourea, and urea are analytical pure grade which purchased from Aladdin online and used without further purification.

2.2 Preparation of Bi@C materials

The aerogel was prepared by cross-linking sodium alginate through Bi ions to form a hydrogel, followed by freeze-drying and subsequent pyrolysis to synthesize Bi@C composites. In a typical synthesis, a proper amount of SA (4 g) and thiourea (8.5 g) were decentralized in 200 mL deionized water and stirring vigorously for 12 h to form a transparent solution. The prepared transparent solution was added dropwise with a medical syringe to a pre-prepared 200 mL solution of 0.1 M bismuth nitrate under continuous stirring. This process facilitated the rapid formation of hydrogel spheres, which were subsequently left undisturbed for 6 h. The hydrogel beads (Bi-alg) were collected by filtration, followed by rinsing with deionized water to remove free impurities. Subsequently, they were placed in a refrigerator set at -50 °C for 24 h to facilitate the transformation into Bi-alg aerogels through a freeze-drying process. Finally, the dried Bi-alg aerogel was carbonized at 600 °C for 1 h under N₂ atmosphere (5 °C·min⁻¹, 80 mL·min⁻¹ N₂). After cooling in flowing N₂ environment, the obtained samples were recorded as Bi@C.

2.3 Preparation of flowers-like $\text{Bi}_2\text{O}_2\text{CO}_3@\text{C}$

$\text{Bi}_2\text{O}_2\text{CO}_3@\text{C}$ composites were synthesized using $\text{Bi}@\text{C}$ precursor via traditional hydrothermal methods. In subsequently, 0.5 g graphene and 0.4 g urea were dissolved in 70 mL deionized water and ultrasonic dispersion for 10 min. Then, 0.5 g $\text{Bi}@\text{C}$ composite was added to the mixture and stirred for 60 min to make the mixture dispersion homogeneously. Subsequently, the mixture was transformed to a Teflon-lined autoclave and kept at 180 °C for 10 h. The finally obtained black precipitate was collected by centrifugation and washed thoroughly with deionized water and ethanol more than three times, and dried in a vacuum at 70 °C overnight. The dried black powder obtained was labeled as $\text{Bi}_2\text{O}_2\text{CO}_3@\text{C}$.

2.4 Materials characterization

The phase structure of the as-prepared samples was measured by XRD (Rigaku D/max 2500) operating at 40 kV and 15 mA using Cu K α 1 radiation ($\lambda = 1.541 \text{ \AA}$, step size = 0.02° , $5^\circ \cdot \text{min}^{-1}$ from 10° to 80°). X-ray photoelectron spectroscopy (XPS, Thermo Scientific K-Alpha) and Raman (Jobin Yvon, T6400) were used to observe the phase composition. The microstructure was investigated by scanning electron microscopy (SEM, Hitachi Su8010) and transmission electron microscopy (TEM, JEOL-2100). Thermogravimetric analysis (TGA, Mettler-Toledo Model TGA/DSC1) and Brunauer–Emmett–Teller (BET, Micro-metrics Instrument Corporation) were further conducted.

2.5 Electrochemical measurements

The CR2025-type coin cells were assembled for the electrochemical measurements. The working electrode consists of active materials (80 wt%, $\text{Bi}_2\text{O}_2\text{CO}_3@\text{C}$), Super P (10 wt%) and polyvinylidene difluoride (PVDF) binder (10 wt%). LiPF_6 (1.0 M) dissolved in ethylene carbonate/diethyl carbonate/- dimethyl carbonate (EC/DEC/DMC) (1:1:1 in vol%) was used as electrolyte. The mass loading of active material was about $1.2\text{--}1.5 \text{ mg}\cdot\text{cm}^{-2}$. The metallic Li was employed as the counter electrode for the half cell. For assembled the full cell, the LMLC was used as cathode, which synthesized according to a previous reported, and the mass ratio of the $\text{Bi}_2\text{O}_2\text{CO}_3@\text{C}$ anode and LMLC cathode is 0.354 [43]. Furthermore, the pre-Li of $\text{Bi}_2\text{O}_2\text{CO}_3@\text{C}$ anode was conducted before assembled full cell. The cyclic voltammetry (CV) and electrochemical impedance spectroscopy test were performed on electrochemical work-station (CHI660E) between 0.01 and 3.0 V (vs. Li/Li^+). The Li storage performances were conducted on LAND-BT2013A measurement system.

3 Results and discussion

$\text{Bi}_2\text{O}_2\text{CO}_3@\text{C}$ composites were synthesized via two processes of annealing of Bi-alg in concert with a subsequent hydrothermal process, as depicted in Fig. 1a. The intricate microstructure properties of the $\text{Bi}_2\text{O}_2\text{CO}_3@\text{C}$ composites were examined through SEM and TEM observations. Figure 1b–d depicts the flower-like aggregates morphology of $\text{Bi}_2\text{O}_2\text{CO}_3$ and the composite structure of $\text{Bi}_2\text{O}_2\text{CO}_3@\text{C}$. Obviously, nanosheets self-assembled and anchored on a carbon substrate to form the $\text{Bi}_2\text{O}_2\text{CO}_3@\text{C}$ composite structure during the hydrothermal process. Additionally, rough and concave surfaces, as well as porosity, were observed within the carbon matrix due to the release of gases during the pyrolysis process (Fig. 1c). SEM images reveal a relatively homogeneous distribution of flower-like nanosheets on the surface of the carbon matrix, with graphene randomly dispersed among the carbon matrix particles. The size of the flower-like $\text{Bi}_2\text{O}_2\text{CO}_3$ aggregates is between $0.5\text{--}2 \mu\text{m}$ in diameter. The $\text{Bi}_2\text{O}_2\text{CO}_3$ nanosheets obtained were further elucidated through TEM analysis, as depicted in Fig. 1e. The size of the nanosheets is distributed in the range of $200\text{--}600 \text{ nm}$. The interplanar distance is 0.269 nm , which is corresponding to (022) plane of $\text{Bi}_2\text{O}_2\text{CO}_3$. Furthermore, the elemental mappings in Fig. 1h, i indicate that $\text{Bi}_2\text{O}_2\text{CO}_3$ is distributed on the carbon-based substrate. Corresponding energy dispersive spectroscopy (EDS) spectrum (Fig. 1j) validates the composition of $\text{Bi}_2\text{O}_2\text{CO}_3@\text{C}$, primarily consisting of Bi, C and O. The phase structure was further confirmed by XRD results.

The phase structural of the $\text{Bi}_2\text{O}_2\text{CO}_3@\text{C}$ samples prepared in this work were conducted using powder XRD, followed by a detailed Rietveld refinement analysis (Fig. 2a). The detected diffraction peaks exhibit a remarkable agreement with the expected pattern of the pure orthorhombic structure with a space group of Pn21a ($a = 10.94 \text{ \AA}$, $b = 27.32 \text{ \AA}$, $c = 10.94 \text{ \AA}$). Clearly, the primary diffraction peaks can be attributed to the crystalline structure of $\text{Bi}_2\text{O}_2\text{CO}_3$ (PDF No. 84–1752). In addition to the mentioned diffraction peaks, no additional diffraction peaks were observed, confirming the high content of $\text{Bi}_2\text{O}_2\text{CO}_3$ in the samples consisting of a single-phase orthorhombic structure. As illustrated in Fig. 2b, the configuration of the $\text{Bi}_2\text{O}_2\text{CO}_3$ structure exhibited a stacked arrangement with alternating layer packages oriented perpendicular to the [001] axis. Within each layer, there existed a double sublayer composed of oxygen atoms and carbonate ions, respectively. The metal atoms occupied slightly distorted octahedral sites embedded within the double sublayer, while distinct layer packages were separated by a van der Waals gap. This

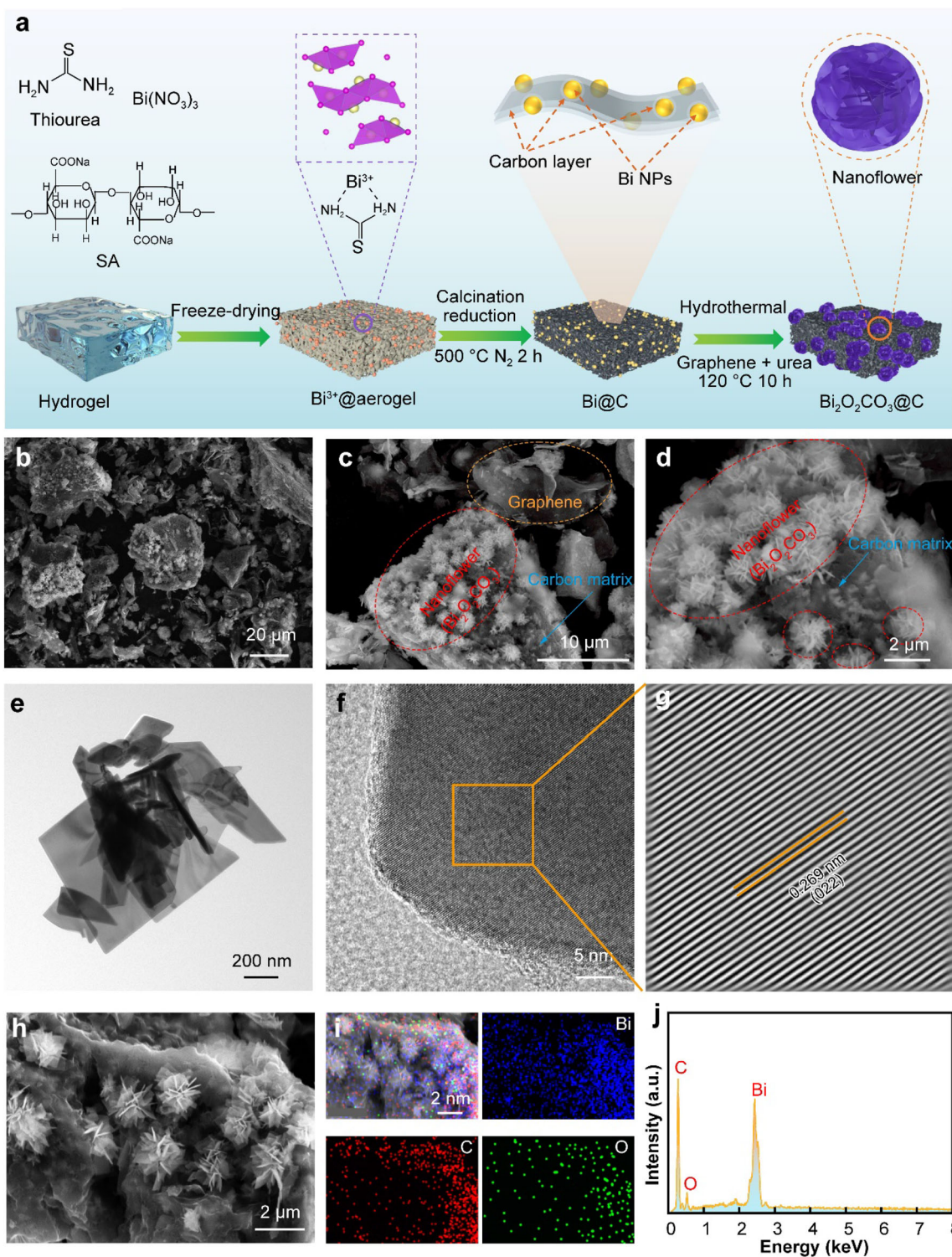


Fig. 1 **a** Schematic illustration of fabrication of $\text{Bi}_2\text{O}_2\text{CO}_3@\text{C}$; **b–d** SEM images with different magnification of $\text{Bi}_2\text{O}_2\text{CO}_3@\text{C}$; **e** TEM image, **f** HRTEM image and **g** local magnified HRTEM image of $\text{Bi}_2\text{O}_2\text{CO}_3$ nanosheet of $\text{Bi}_2\text{O}_2\text{CO}_3@\text{C}$; **h, i** elemental mapping of $\text{Bi}_2\text{O}_2\text{CO}_3@\text{C}$; **j** EDS result of $\text{Bi}_2\text{O}_2\text{CO}_3@\text{C}$

unique channel structure facilitated the diffusion and storage of ions, while also serving as a buffer for accommodating volumetric changes during the electrochemical reaction.

Raman spectroscopic investigation was performed to investigate the structural features of $\text{Bi}_2\text{O}_2\text{CO}_3@\text{C}$ (Fig. 2c). Two peaks were observed in Raman spectrum at 1360 and 1567 cm^{-1} , corresponding to the D-band

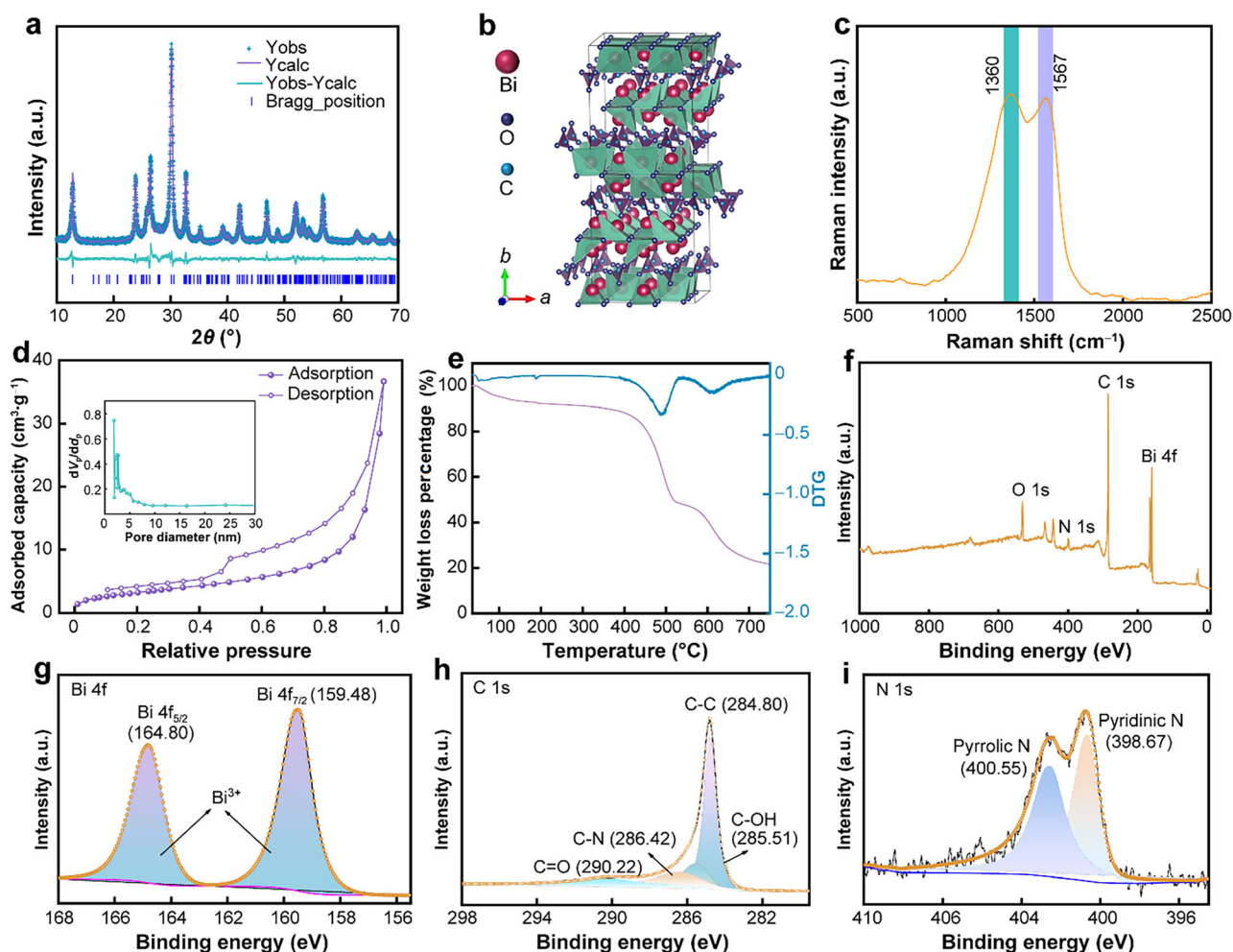


Fig. 2 a XRD pattern of $\text{Bi}_2\text{O}_2\text{CO}_3@\text{C}$; b schematic illustration of crystal structure of $\text{Bi}_2\text{O}_2\text{CO}_3$; c Raman spectrum; d N_2 adsorption–desorption isotherm; e TGA curve; XPS spectra: f survey spectrum, g Bi 4f, h C 1s and i N 1s

(disordered graphite) and G-band (crystalline graphite), respectively [44]. The presence of disorder nature in $\text{Bi}_2\text{O}_2\text{CO}_3@\text{C}$, which contributes to enhanced electrochemical performance and safety in LIBs (as lithiation occurs at higher voltages compared to graphitic carbon) [45], is supported by the calculated I_D/I_G ratio of 1.01 derived from the Raman spectrum. To further investigate the porous structure and the associated pore size distribution of the obtained samples, N_2 adsorption–desorption isotherms were employed. As shown in Fig. 2d, it can be observed that $\text{Bi}_2\text{O}_2\text{CO}_3@\text{C}$ demonstrate a combination of type-I and type-IV isotherms, indicating the presence of a micro-mesoporous structure [46]. The specific surface area of $\text{Bi}_2\text{O}_2\text{CO}_3@\text{C}$ was measured to be $70 \text{ m}^2 \cdot \text{g}^{-1}$, indicating its considerable surface area. The pore size distribution trend of $\text{Bi}_2\text{O}_2\text{CO}_3@\text{C}$ was confirmed to be predominantly microporous by the Barrett–Joyner–Halenda (BJH) analysis (Inset of Fig. 2d). The mesopores with sizes ranging

from 2 to 5 nm provide significant advantages in achieving superior contact with the electrolyte solution.

TGA of $\text{Bi}_2\text{O}_2\text{CO}_3@\text{C}$ was conducted under an O_2 atmosphere, as shown in Fig. 2e. The weight loss of $\text{Bi}_2\text{O}_2\text{CO}_3@\text{C}$ was observed to occur in three distinct stages. There was a slight mass loss of the sample in the preliminary period of temperature increase (before $200 \text{ }^\circ\text{C}$), which can be attributed to the evaporation of water within the composite [47, 48]. In the temperature range of $200\text{--}640 \text{ }^\circ\text{C}$, a notable reduction in weight was observed, indicating the combustion decomposition of carbon within the composites [49]. Accordingly, the calculated content of carbon and $\text{Bi}_2\text{O}_2\text{CO}_3$ in the composites is approximately 43% and 48%, respectively. The gravimetric loss in the third stage is a consequence of the thermal decomposition of $\text{Bi}_2\text{O}_2\text{CO}_3$ into Bi_2O_3 and CO_2 .

XPS was employed to investigate the bonding information and chemical constitutions of $\text{Bi}_2\text{O}_2\text{CO}_3@\text{C}$. The survey spectrum (Fig. 2f) results reveal that the elements

C, O, N and Bi are present in the Bi₂O₂CO₃@C composites, which is consistent with EDS maps in Fig. 1. High-resolution XPS spectrum of Bi 4f in Fig. 2g exhibits two peaks at 164.80 and 159.48 eV, which are ascribed to Bi 4f_{5/2} and Bi 4f_{7/2}, respectively [42, 50]. The deconvolution for C 1s spectra (Fig. 2h) of all Bi₂O₂CO₃@C compounds is divided into four peaks derived from C=C, C–OH, C–N and C=O, respectively [51]. High-resolution XPS spectra of N 1s of Bi₂O₂CO₃@C are presented in Fig. 2i, wherein the two peaks centered at 400.55 and 398.67 eV were fitted. These peaks associated with pyrrolic-N and pyridinic-N components, respectively [52, 53]. The introduced N element is conducive to improve the electrical conductivity of the composites and provides active sites for Li storage.

The Li⁺ storage behavior of Bi₂O₂CO₃@C composites was explored using half coin cells within a potential window of 0.1–3.0 V. The electrochemical reactions were elucidated by the cathodic and anodic peaks observed in the initial five CV curves obtained at a scan rate of 0.1 mV·s⁻¹ (Fig. 3a). During the first cathodic scan, a series of reduction peaks ranging from 0.09–0.84 V are observed, which can be attributed to the stepwise lithiation process of Bi. However, these peaks disappear in the subsequent cycles. This process involves the formation of the solid electrolyte interfacial film (SEI layer), followed by the chemical reaction of the formation of Li₃Bi. The primary reaction equations corresponding to these processes can be described as $\text{Bi} + 3\text{Li}^+ + 3\text{e}^- \rightarrow \text{Li}_3\text{Bi}$ [54]. In the anodic scan, the observed oxidation peak at

approximately 0.98 V is primarily attributed to the dealloying process of Bi, which can be represented by the reaction $\text{Li}_3\text{Bi} \rightarrow \text{Bi} + 3\text{Li}^+ + 3\text{e}^-$ [55]. The lithiation process of Bi₂O₂CO₃ leads to the degradation of the electrolyte and the generation of the SEI, resulting in an irreversible reduction in the specific capacity during the initial cycle [56]. However, upon the formation of the SEI film, it can be observed from the highly overlapped CV curves in the second to fifth cycles that the Bi₂O₂CO₃@C composite possesses excellent cycling stability. Furthermore, the appearance of broad and weak redox peaks at ~ 0.16 V is associated with the accommodation of Li⁺ during the interface reaction [57].

The electrochemical characteristics of Bi₂O₂CO₃@C composites can be evaluated by performing galvanostatic charge–discharge experiments within the voltage window of 0.01–3.00 V. Figure 3b illustrates the galvanostatic charge–discharge profiles of the Bi₂O₂CO₃@C cathode during the 1st, 2nd, 4th, 6th, 8th and 10th cycles, at a current density of 0.1 A·g⁻¹. As depicted in Fig. 3b, the discharge profiles display two distinct plateaus at 0.69 and 0.08 V, which can be attributed to the processes of Bi → Li₃Bi and the interface reaction during the electrochemical reaction at a current density of 0.1 A·g⁻¹. Similarly, the charge profiles reveal voltage plateaus at 0.89 and 0.12 V, which are associated with the dealloying process and interface reaction. These observations are in strong agreement with the CV measurements. In the initial cycle, the discharge and charge capacities are recorded as 1183 and

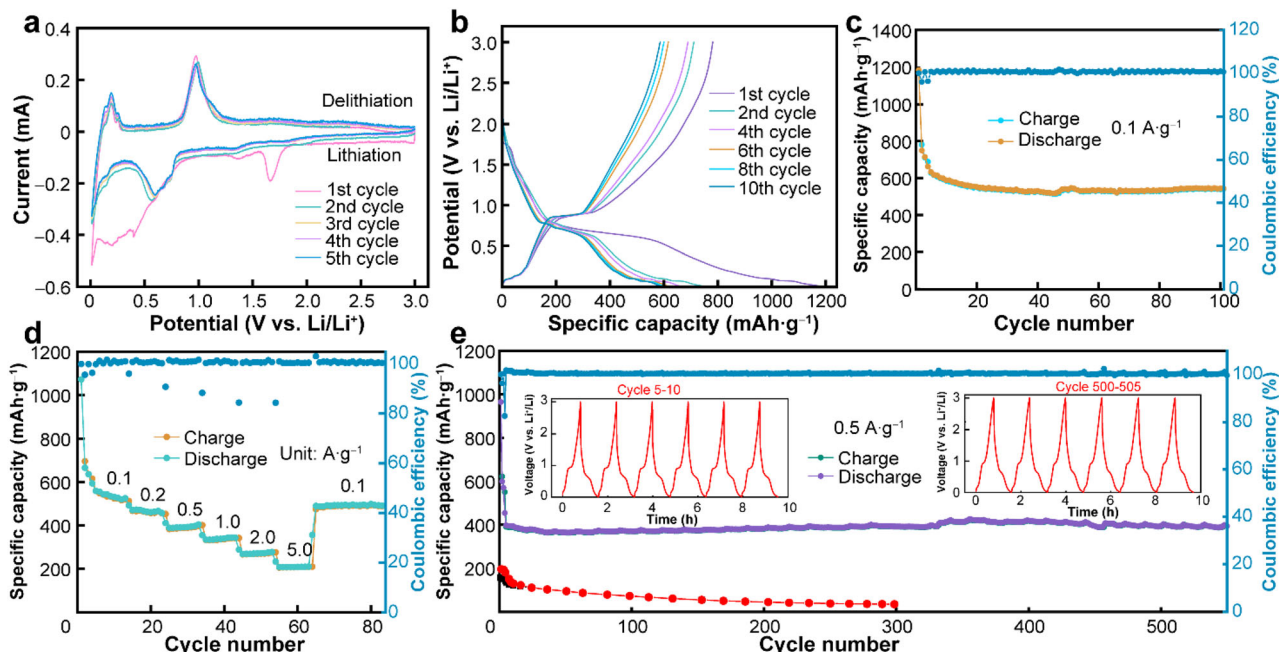


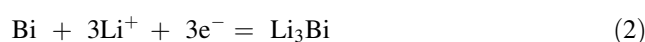
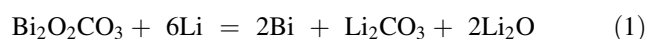
Fig. 3 a CV curves of Bi₂O₂CO₃@C at a scan rate of 0.1 mV·s⁻¹; b GCD curves tested at 0.1 A·g⁻¹; c cycling properties at 0.1 A·g⁻¹; d c-rate performance at various current densities; e long-term cycling properties at 0.5 A·g⁻¹

781 mAh·g⁻¹, respectively. Actually, the discharge capacity of Bi-based anode materials all shows rapid decline due to the formation of the SEI layer during the alloying or conversion reaction procedure, which is consistent with the reported results [54, 55]. With increasing cycling, the specific capacity during discharge reaches a stable state, while the Coulombic efficiency stays at around 98% from the second cycle. The cycling behavior of the Bi₂O₂CO₃@C was investigated at a current density of 0.1 A·g⁻¹, as depicted in Fig. 3c. At a current density 0.1 A·g⁻¹, the discharge specific capacity of Bi₂O₂CO₃@C stabilized at 547 mAh·g⁻¹ after 100 cycles, while the Coulombic efficiency remained above 99% throughout the duration of the experiment, suggesting the excellent reversibility of the anode materials. Additionally, the energy density of the Bi₂O₂CO₃@C cathode is 396 mWh·g⁻¹ during the first cycles, decreasing to 343 mWh·g⁻¹ after 100 cycles at 0.1 A·g⁻¹. It has been reported in the literature that bare Bi₂O₂CO₃ anode was tested in cycling at 0.5 A·g⁻¹ and the discharge specific capacity of the battery decayed from 156 mAh·g⁻¹ in the first cycle to 34.8 mAh·g⁻¹ after 300 cycles, as shown in Fig. 3e [58]. During the extended cycle test at an elevated current density to 0.5 A·g⁻¹, a remarkable reversible capacity of 394 mAh·g⁻¹ was maintained experience 550 galvanostatic charge–discharge (GCD) cycles (Fig. 3e). The rate performance of Bi₂O₂CO₃@C was further investigated under various current densities, such as 0.1, 0.2, 0.5, 1.0, 2.0, 5.0 A·g⁻¹, as shown in Fig. 3d. When operating at a current density of 0.1 A·g⁻¹, the capacity of Bi₂O₂CO₃@C experienced a decline in the initial ten cycles, which can be attributed to an activation (de)lithiation process. However, despite this initial decrease, the average Coulombic efficiency consistently maintained a stable value of approximately 98%. Remarkably, the Bi₂O₂CO₃@C composite exhibited impressive reversible capacities of 466.1, 404.3, 343.3, 276.9, 209.8 and 498.0 mAh·g⁻¹ at 0.5, 1.0, 2.0, 5.0 and 0.1 A·g⁻¹, respectively. These results collectively highlight the exceptional stability, reversibility, and high Coulombic efficiency of the Bi₂O₂CO₃@C composite, signifying its promising potential as a prospective anode material for LIBs.

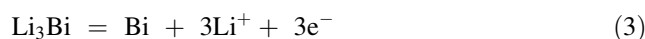
To further elucidate the Li storage mechanism of the Bi₂O₂CO₃@C anode, it was incorporated as an anode material (loaded onto a circular pure beryllium disk) and assembled it with a Li foil cathode in a specially designed setup. This method was conducted to recording the phase variation of the Bi₂O₂CO₃@C composite material in real-time during the battery charge–discharge cycling tests, as shown in Fig. 4. As the discharge process proceeds, the diffraction peaks corresponding to Bi₂O₂CO₃ (24.4°, 30.7° and 33.2°) progressively decrease and eventually

disappeared completely. The decreased peak intensity corresponds to the conversion of Bi₂O₂CO₃ into discharge products, namely Bi (27.7° and 40.2°), and Li₃Bi (23.5°, 38.5° and 45.3°). The characteristic diffraction peaks associated with Bi during the charging and discharging process (corresponding to the position of the voltage around 0.7 V of the charging/discharging curve) can be clearly observed in the figure. This observation confirmed the conversion of Bi₂O₂CO₃ into Bi during the discharge phase. Conversely, during the charging phase, the noticeable peaks at 23.5°, 38.5° and 45.3° gradually diminish, confirming the phase transition of Li₃Bi. The diffraction peaks of Bi₂O₂CO₃ disappeared when the charge reached below 0.7 V during the initial discharge and did not reappear during the subsequent charging and discharging process, which indicates that the transformation reaction of the Bi₂O₂CO₃@C composite material is irreversible within the cycling process. The underlying reaction mechanism of the Bi₂O₂CO₃@C composites could be described as follows Eqs. (1-3)

In the discharge process:



In the charge process:



The phase transition process was further illustrated by the 3D contour plot of in situ XRD pattern, as depicted in Fig. 4b. The significant changes in peak intensity (indicated by the arrows) within the plot confirmed the generation of Bi and Li₃Bi as the final discharge products. Enlarged XRD in Fig. 4c presents detailed variations in peak intensity within different ranges. In summary, the charge storage mechanism of Bi₂O₂CO₃@C composites as an anode for LIBs was determined using in situ XRD characterization techniques. This mechanism involves the initial irreversible conversion of Bi₂O₂CO₃ to Bi, followed by an alloying reaction between Bi and Li⁺, resulting in the formation of Li₃Bi, which is subsequently dealloying to regenerate Bi.

CV at various scan rates (0.2–1.0 mV·s⁻¹) were performed for the purpose of further investigating the Li storage mechanism of Bi₂O₂CO₃@C composites. CV profiles of the Bi₂O₂CO₃@C anode exhibited similar shapes at different scanning rates, indicating rapid kinetic behavior [59], as illustrated in Fig. 5a. The equation governing the relationship between the peak current (*i*, mA) and scan rate (*v*, mV⁻¹) is given by Eq. (4), with *a* and *b* being adjustable parameters that can be determined by fitting a lg*v*–lg*i* curve. The peak currents of the reduction peak (Peak I) and oxidation peak (Peak II) were utilized in

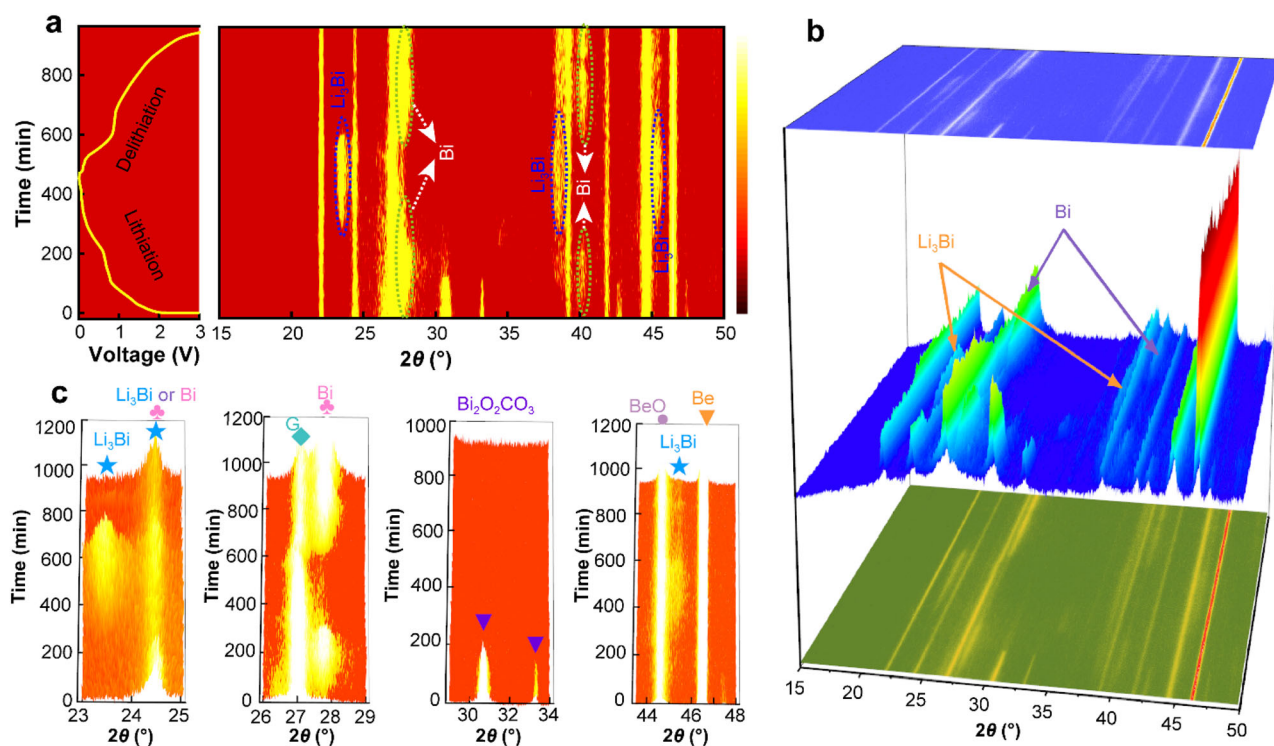


Fig. 4 **a** The 1st charge/discharge cycle curves and corresponding in situ 2D maps of XRD; **b** 3D map with full contour maps; **c** individual contour maps of Bi₂O₂CO₃@C anode in the 1st discharge/charge cycle

Eq. (5) to determine the reaction kinetic parameter b value for Bi₂O₂CO₃@C composites (Fig. 5a). A reaction process that is primarily governed by diffusion is linked to the b value of ~ 0.5 , while a reaction process primarily controlled by capacitance is typically associated with the b value close to 1 [60]. By performing a linear regression analysis, Fig. 5b was generated, and the obtained b values for Peak I and Peak II are 0.69 and 0.60, respectively, implying the prevalence of a capacitive dominant process in the Bi₂O₂CO₃@C electrode with exceptional kinetic properties. It is widely acknowledged that Eqs. (4, 5) can effectively differentiate between the contributions of pseudo-capacitive control behavior and diffusion control behavior. Figure 5c presents the contribution of the pseudo-capacitor control process at a scan rate of 0.8 mV·s⁻¹, which account for 56.27%. Notably, the pseudo-capacitive contributions exhibit a significant increase with the escalation of scan rates (Fig. 5d), thereby providing a possible explanation for the remarkable rate performance observed. Consequently, the involvement of capacitance contribution plays a significant role in the (de)lithiation process of the Bi₂O₂CO₃@C electrode, resulting in enhanced rate and capacity performance of the Bi₂O₂CO₃@C composites.

$$i = av^b \quad (4)$$

$$i(V) = k_1v + k_2v^{0.5} \quad (5)$$

where i , v , $i(V)$, k_1v and $k_2v^{0.5}$ represent the peak current, scan rate, total current, surface induced capacitive-controlled current and diffusion-controlled current, respectively.

The Nyquist plots of the Bi₂O₂CO₃@C electrode at the initial and 100th cycled states are presented in Fig. 5e, wherein the semicircle observed at medium and high-frequency ranges signifies the charge transfer resistance (R_{ct}) and surface resistance (R_s), while the oblique line corresponds to the Warburg resistance (R_w). After 100 cycles, the impedances of the Bi₂O₂CO₃@C electrode were observed to decrease in comparison with the fresh state, which is attributed to the formation of the SEI layer. The SEI is facilitated by the presence of flexible carbon multi-chambers and interconnected architectures [61]. Additionally, the reduced particle size resulting from repeated interaction with Li⁺ also contributes to the improved impedance behavior. According to the concept that ideal pseudo-capacitive materials exhibit alternating current (AC) impedance characteristics with a phase angle of 90° or less in the Nyquist plot [62], the Bi₂O₂CO₃@C electrode demonstrates a steeper slope in the low-frequency region, as depicted in Fig. 5e. In the corresponding Bode plots (Fig. 5f), the phase angle of Bi₂O₂CO₃@C approaches nearly 90° at a frequency near 0.01 Hz. By employing the commonly used equivalent circuit for analysis, it becomes evident that the influence of Warburg impedance accounts

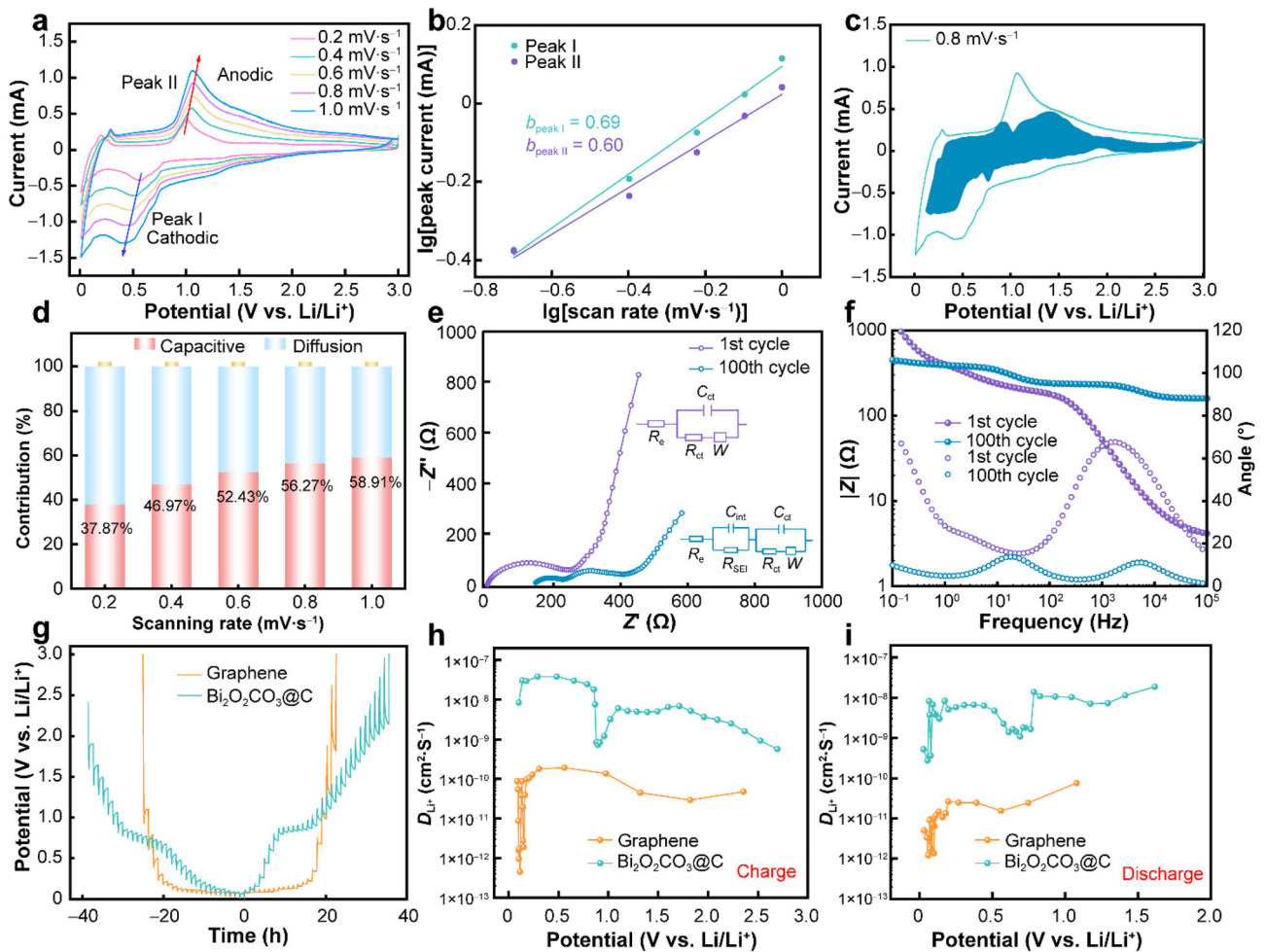


Fig. 5 **a** CV profiles of $\text{Bi}_2\text{O}_2\text{CO}_3@\text{C}$ at different scan rates; **b** $\lg I$ - $\lg v$ curve; **c** capacitive separation at $0.8 \text{ mV}\cdot\text{s}^{-1}$ of $\text{Bi}_2\text{O}_2\text{CO}_3@\text{C}$ electrode; **d** contribution ratios of capacitive; **e** Nyquist plot and **f** corresponding bode plot of $\text{Bi}_2\text{O}_2\text{CO}_3@\text{C}$ after different cycles; **g** GITT curves; **h**, **i** variation of D_{Li^+} values during charge and discharge

for the slope observed in the high-frequency range of $\text{Bi}_2\text{O}_2\text{CO}_3@\text{C}$, approaching 45° – 60° . The Warburg impedance is associated with the diffusion process, explaining the role of the electrochemical diffusion process in the behavior of $\text{Bi}_2\text{O}_2\text{CO}_3@\text{C}$.

To better understand the characterization of Li^+ diffusion behavior in $\text{Bi}_2\text{O}_2\text{CO}_3@\text{C}$ electrode, the galvanostatic intermittent titration technique (GITT) was performed to evaluate the (de)lithiation process within the cell. The GITT analysis was conducted to determine accurate Li^+ diffusion rates in $\text{Bi}_2\text{O}_2\text{CO}_3@\text{C}$ under a current density of $0.1 \text{ A}\cdot\text{g}^{-1}$, the intermittent discharge/charge procedure lasting 10 min, and subsequent resting intervals of 60 min (as illustrated in Fig. 5g), the Li^+ diffusion coefficient (D_{Li^+}) was determined using Eq. (6) [32, 34]:

$$D_{\text{Li}^+} = \frac{4}{\pi\tau} \left(\frac{m_{\text{B}} V_{\text{m}}}{M_{\text{B}} S} \right)^2 \left(\frac{\Delta E_{\text{S}}}{\Delta E_{\tau}} \right)^2 \quad (6)$$

where τ , m_{B} , M_{B} , V_{m} and S represent relaxation time, weight of active material, molar mass, molar volume and active surface area, respectively. ΔE_{S} is the voltage change in response to a pulse, and ΔE_{τ} is the voltage change associated with constant current charging (discharging). And the values of ΔE_{S} and ΔE_{τ} can be directly obtained from the GITT curves. As shown in Fig. 5h, i, the measured diffusion coefficient (D_{Li^+}) for the charging process of $\text{Bi}_2\text{O}_2\text{CO}_3@\text{C}$, which ranges from 10^{-10} to $10^{-8} \text{ cm}^2\cdot\text{s}^{-1}$. Additionally, the D_{Li^+} value for the discharging process is slightly lower than the charging process. For visual comparison, graphene was subjected to GITT tests under identical conditions. The D_{Li^+} range for graphene during the charging process is from 10^{-13} to $10^{-10} \text{ cm}^2\cdot\text{s}^{-1}$, while the D_{Li^+} range for the discharging process is from 10^{-12} to $10^{-10} \text{ cm}^2\cdot\text{s}^{-1}$. The higher D_{Li^+} values obtained can be attributed to the enhanced reactivity of the flower-like $\text{Bi}_2\text{O}_2\text{CO}_3$ nanosheet and the short Li^+

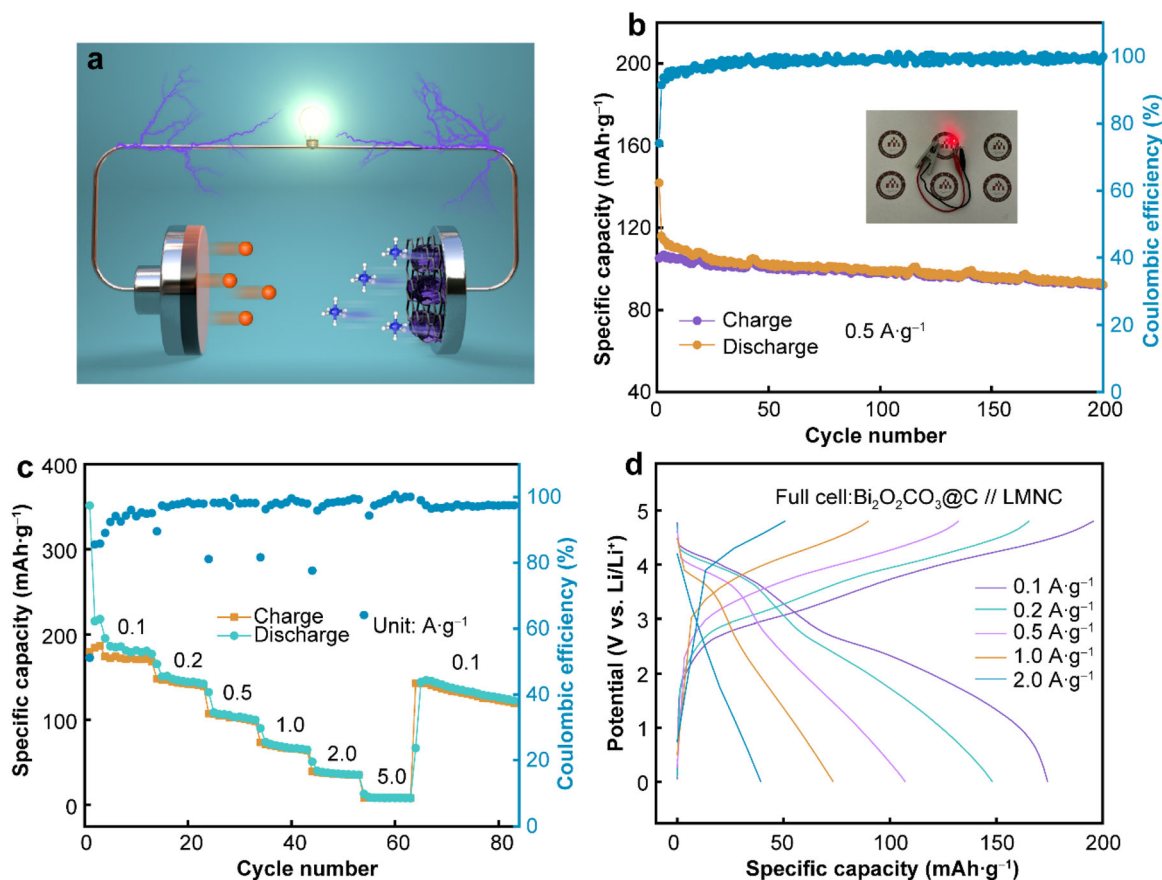


Fig. 6 **a** Schematic illustration of $\text{Bi}_2\text{O}_2\text{CO}_3@C$ /LMLC full cell; **b** cycle performance at $0.5 \text{ A}\cdot\text{g}^{-1}$ and (inset) an optical image showcasing a full LIB energizing a red-LED; **c** discharge performance under different current densities; **d** GCD profiles with varied current densities

diffusion distance within $\text{Bi}_2\text{O}_2\text{CO}_3@C$. In summary, the incorporation of the in situ grown flower-like $\text{Bi}_2\text{O}_2\text{CO}_3$ nanosheet within the carbon matrix facilitates remarkable Li^+ storage kinetics.

To confirm the feasibility of integrating $\text{Bi}_2\text{O}_2\text{CO}_3@C$ into complete LIBs, LMLC was utilized as the cathode to assemble a full cell. The schematic diagram of the full cell arrangement is depicted in Fig. 6a. The full cell was initially charged to 4.8 V for activation and subsequently exhibited a rechargeable capacity of $174.1 \text{ mAh}\cdot\text{g}^{-1}$ at a rate of $0.1 \text{ A}\cdot\text{g}^{-1}$. The initial Coulombic efficiency was recorded to be 91.4% (Fig. 6b). The irreversible capacity can be attributed to the formation of the cathode-electrolyte interface (CEI) on the cathode side, while the capacity degradation on the anode side follows a typical pattern. The capacity was consistently maintained at around $100 \text{ mAh}\cdot\text{g}^{-1}$ after 200 cycles at a current density of $0.5 \text{ A}\cdot\text{g}^{-1}$, as depicted in Fig. 6b. Constant-current discharging at various current densities (Fig. 6d) demonstrated substantial capacity delivery for the full cell across different current densities, with values of 174.1, 148.1, 107.2, 73.3 and $39.2 \text{ mAh}\cdot\text{g}^{-1}$ at 0.1, 0.2, 0.5, 1 and

$2 \text{ A}\cdot\text{g}^{-1}$, respectively. Upon returning to a current density of $0.1 \text{ A}\cdot\text{g}^{-1}$, the reversible capacity remarkably recovered to $146.3 \text{ mAh}\cdot\text{g}^{-1}$, highlighting the impressive ability of the $\text{Bi}_2\text{O}_2\text{CO}_3@C$ electrode to withstand varying rates in the full cell. Moreover, the Coulombic efficiency reaches more than 98%, indicating that the full cells composed of $\text{Bi}_2\text{O}_2\text{CO}_3@C$ /LMLC possess promising prospects in low current density application domains. Additionally, compared to previously reported anodes, $\text{Bi}_2\text{O}_2\text{CO}_3@C$ exhibits excellent performance in full cell tests (Table S1). According to Fig. 6b, it is evident that a full Li-ion battery can effortlessly power a red-light emitting diode (LED). The remarkable electrochemical performance observed in the full Li-ion battery suggests the possibility of a novel anode for LIBs, indicating its potential feasibility.

4 Conclusion

Flower-like $\text{Bi}_2\text{O}_2\text{CO}_3$ composites anchored on a carbon substrate were successfully prepared using a simple method and employed as a highly promising anode material for

LIBs. Anchoring flower-like $\text{Bi}_2\text{O}_2\text{CO}_3$ nanosheets onto a carbon substrate is beneficial for enhancing the electrical conductivity of $\text{Bi}_2\text{O}_2\text{CO}_3$ and mitigate both volume expansion and agglomeration of the nanosheets. The unique and novel flower-like structure of the $\text{Bi}_2\text{O}_2\text{CO}_3$ @C anode enables it to provide a stable reversible capacity of $547 \text{ mAh}\cdot\text{g}^{-1}$ at $0.1 \text{ A}\cdot\text{g}^{-1}$ after 100 cycles. Additionally, the composites exhibit excellent rate performance, with specific capacities of 548.1, 466.1, 404.3, 343.3, 276.9, 209.8 and $498.0 \text{ mAh}\cdot\text{g}^{-1}$ at current densities of 0.1, 0.5, 1.0, 2.0, 5.0 and $0.1 \text{ A}\cdot\text{g}^{-1}$, respectively. Even after 550 cycles at a current density of $0.5 \text{ A}\cdot\text{g}^{-1}$, it maintains a reversible specific capacity of $394 \text{ mAh}\cdot\text{g}^{-1}$. The Li-ion storage mechanism and kinetic reaction of the $\text{Bi}_2\text{O}_2\text{CO}_3$ @C composites were explored using in situ XRD, scanning method and GITT. Additionally, the $\text{Bi}_2\text{O}_2\text{CO}_3$ @C//LMLC full cell achieved an exceptional discharge specific capacity of nearly $100 \text{ mAh}\cdot\text{g}^{-1}$ at $0.5 \text{ A}\cdot\text{g}^{-1}$, demonstrating its practical application potential. It also maintained a high Coulomb efficiency of 99% over 200 cycles at $0.5 \text{ A}\cdot\text{g}^{-1}$. The exciting findings of this study have the potential to significantly advance the development and construction of high-performance negative electrode materials for advanced LIBs and other rechargeable batteries.

Acknowledgements This study was financially supported by Yunnan Fundamental Research Projects (Nos. 202401AU070164 and 202101AU070157), the National Natural Science Foundation of China (No. 52064028) and Yunnan Provincial Major Science and Technology Special Plan Projects (No. 202202AF080002).

Declarations

Conflict of interests The authors declare that they have no conflict of interest.

References

- [1] Tarascon JM, Armand M. Issues and challenges facing rechargeable lithium batteries. *Nature*. 2001;414:359. <https://doi.org/10.1038/35104644>.
- [2] Simon P, Gogotsi Y. Perspectives for electrochemical capacitors and related devices. *Nat Mater*. 2020;19:1151. <https://doi.org/10.1038/s41563-020-0747-z>.
- [3] Yan J, Cui Y, Xie M, Yang GZ, Bin DS, Li D. Immobilizing redox-active tricycloquinazoline into a 2D conductive metal-organic framework for lithium storage. *Angew Chem Int Ed*. 2021;133:24672. <https://doi.org/10.1002/anie.202110373>.
- [4] Zhan HB, Liu SQ, Wang Q, Cao ML, Ma YN, Zhang CK, Li J. Development of lithium manganese iron phosphate cathode material for lithium-ion batteries. *Chin J Rare Met*. 2023;47(12):1669. <https://doi.org/10.13373/j.cnki.cjrm.XY23060002>.
- [5] Liu SY, Zhou YH, Zhang YB, Xia SJ, Li Y, Zhou X, Qiu B, Shao GJ, Liu ZP. Surface yttrium-doping induced by element segregation to suppress oxygen release in Li-rich layered oxide cathodes. *Tungsten*. 2022;4:336. <https://doi.org/10.1007/s42864-022-00165-2>.
- [6] Geng KQ, Yang MQ, Meng JX, Zhou LF, Wang YQ, Dmytro S, Zhang Q, Zhong SW, Ma QX. Engineering layered/spinel heterostructure via molybdenum doping towards highly stable Li-rich cathodes. *Tungsten*. 2022;4:323. <https://doi.org/10.1007/s42864-022-00173-2>.
- [7] Zishan A, Cai ZF, Wang S, Wang HC, Ma YZ, Song GS, Zhang SH, Yang WD, Muhammad I, Wen CE. Enhanced stability and electrochemical properties of lanthanum and cerium co-modified LiVOPO_4 cathode materials for Li-ion batteries. *J Rare Earth*. 2023;41:1590. <https://doi.org/10.1016/j.jre.2022.09.020>.
- [8] Pan QC, Zhang QB, Zheng FH, Liu YZ, Li YP, Ou X, Xiong XH, Yang CH, Liu ML. Construction of MoS_2 /C hierarchical tubular heterostructures for high-performance sodium ion batteries. *ACS Nano*. 2018;12:12578. <https://doi.org/10.1021/acsnano.8b07172>.
- [9] Obrovac MN, Chevrier VL. Alloy negative electrodes for Li-ion batteries. *Chem Rev*. 2014;114:11444. <https://doi.org/10.1021/cr500207g>.
- [10] Bai J, Chen X, Olsson E, Wu HM, Wang SQ, Cai Q, Feng CQ. Synthesis of Bi_2S_3 /carbon nanocomposites as anode materials for lithium-ion batteries. *J Mater Sci Technol*. 2020;50:92. <https://doi.org/10.1016/j.jmst.2020.01.045>.
- [11] Chen JX, Su ZL, Zhao T, Pu GG, Li A, Wang L. Performance of cathode material of high-power lithium-ion battery. *Chin J Rare Met*. 2023;47(12):1756. <https://doi.org/10.13373/j.cnki.cjrm.XY21010027>.
- [12] Lin ZH, Qiu XQ, Zu XH, Zhang XS, Zhong L, Sun SR, Hao SH, Sun YJ, Zhang WL. Ultra-high-rate Bi anode encapsulated in 3D lignin-derived carbon framework for sodium-ion hybrid capacitors. *Rare Met*. 2023;43(3):1037. <https://doi.org/10.1007/s12598-023-02508-5>.
- [13] Dai XJ, Niu XX, Fu WQ, Zheng D, Liu WX, Shi WH, Nai JW, Wu FF, Cao XH. Bismuth-based materials for rechargeable aqueous batteries and water desalination. *Rare Met*. 2021;41(1):287. <https://doi.org/10.1007/s12598-021-01853-7>.
- [14] Li XY, Qu JK, Yin HY. Electrolytic alloy-type anodes for metal-ion batteries. *Rare Met*. 2020;40(2):329. <https://doi.org/10.1007/s12598-020-01537-8>.
- [15] Qiu XL, Wang BY, Jing P, Zhang Y, Zhang M, Wang Q, Chen XC, Zhang Y, Wu H. Bismuth dots imbedded in ultralong nitrogen-doped carbon tubes for highly efficient lithium ion storage. *Inorg Chem Front*. 2020;7:4854. <https://doi.org/10.1039/d0qj01158d>.
- [16] Hong WW, Ge P, Jiang YL, Yang L, Tian Y, Zou GQ, Cao XY, Hou HS, Ji XB. Yolk-shell-structured bismuth@N-doped carbon anode for lithium-ion battery with high volumetric capacity. *ACS Appl Mater Inter*. 2019;11:10829. <https://doi.org/10.1021/acsaami.8b20477>.
- [17] Xiong PX, Bai PX, Li A, Li BF, Cheng MR, Chen YP, Huang SP, Jiang Q, Bu XH, Xu YH. Bismuth nanoparticle@carbon composite anodes for ultralong cycle life and high-rate sodium-ion batteries. *Adv Mater*. 2019;31:-e1904771. <https://doi.org/10.1002/adma.201904771>.
- [18] Qin TT, Chu XF, Deng T, Wang BR, Zhang XY, Dong TW, Li ZM, Fan XF, Ge X, Wang ZZ, Wang P, Zhang W, Zheng WT. Reinventing the mechanism of high-performance Bi anode in aqueous K^+ rechargeable batteries. *J Energ Chem*. 2020;48:21. <https://doi.org/10.1016/j.jechem.2019.12.012>.
- [19] Xue P, Wang NN, Fang ZW, Lu ZX, Xu X, Wang L, Du Y, Ren XC, Bai ZC, Dou SX, Yu GH. Rayleigh-instability-induced bismuth nanorod@nitrogen-doped carbon nanotubes as a long cycling and high rate anode for sodium-ion batteries. *Nano Lett*. 2019;19:1998. <https://doi.org/10.1021/acs.nanolett.8b05189>.



- [20] Shen KX, Zhang ZS, Wang SF, Ru Q, Zhao LZ, Sun LF, Hou XH, Chen FM. Cucumber-shaped construction combining bismuth nanoparticles with carbon nanofiber networks as a binder-free and freestanding anode for Li-ion batteries. *Energy Fuels*. 2020;34:8987. <https://doi.org/10.1021/acs.energyfuels.0c01490>.
- [21] Yang H, Xu R, Yao Y, Ye S, Zhou X, Yu Y. Multicore-shell Bi@N-doped carbon nanospheres for high power density and long cycle life sodium- and potassium-ion anodes. *Adv Funct Mater*. 2019;29:1809195. <https://doi.org/10.1002/adfm.201809195>.
- [22] Li Y, Zhong X, Wu XW, Li MQ, Zhang W, Wang D. Bi/C nanosheet microspheres with an open pore structure as anodes for sodium ion batteries with high capacity, excellent rate performance and long cycle life. *J Mater Chem A*. 2021;9:22364. <https://doi.org/10.1039/d1ta06948a>.
- [23] Yang J, Xian JH, Liu QL, Sun YM, Li GQ. Bi nanoparticles in situ encapsulated by carbon film as high-performance anode materials for Li-ion batteries. *J Energy Chem*. 2022;69:524. <https://doi.org/10.1016/j.jechem.2022.01.026>.
- [24] Wang LC, Światowska J, Dai SR, Cao ML, Zhong ZC, Shen Y, Wang MK. Promises and challenges of alloy-type and conversion-type anode materials for sodium-ion batteries. *Mater Today Energy*. 2019;11:46. <https://doi.org/10.1016/j.mtener.2018.10.017>.
- [25] Wu PF, Shi BY, Tu HB, Guo CQ, Liu AH, Yan G, Yu ZJ. Pomegranate-type Si/C anode with SiC taped, well-dispersed tiny Si particles for lithium-ion batteries. *J Adv Ceram*. 2021;10:1129. <https://doi.org/10.1007/s40145-021-0498-6>.
- [26] Wang Y, Xu XJ, Li FK, Ji SM, Zhao JW, Liu J, Huo YP. Rational design of bismuth metal anodes for sodium-/potassium-ion batteries: recent advances and perspectives. *Batteries*. 2023;9:440. <https://doi.org/10.3390/batteries9090440>.
- [27] Hu ZJ, Li XY, Qu JK, Zhao ZQ, Xie HW, Yin HY. Electrolytic bismuth/carbon nanotubes composites for high-performance sodium-ion battery anodes. *J Power Sour*. 2021;496: 229830. <https://doi.org/10.1016/j.jpowsour.2021.229830>.
- [28] Yin H, Li QW, Cao ML, Zhang W, Zhao H, Li C, Huo KF, Zhu MQ. Nanosized-bismuth-embedded 1D carbon nanofibers as high-performance anodes for lithium-ion and sodium-ion batteries. *Nano Res*. 2017;10:2156. <https://doi.org/10.1007/s12274-016-1408-z>.
- [29] Liu C, Yuan S, Yang Y, Zhao XX, Duan X, Cao B, Wang Q. Prussian blue analogues-derived nitrogen-doped carbon-coated FeO/CoO hollow nanocages as a high-performance anode material for Li storage. *Rare Met*. 2023;42 (12):4070. <https://doi.org/10.1007/s12598-023-02373-2>.
- [30] Xu XJ, Wang ZS, Zhang DC, Zuo SY, Liu J, Zhu M. Scalable one-pot synthesis of hierarchical Bi@C bulk with superior lithium-ion storage performances. *ACS Appl Mater Interfaces*. 2020;12:51478. <https://doi.org/10.1021/acsami.0c14757>.
- [31] Xu XJ, Zhang DC, Wang ZS, Zuo SY, Shen JD, Liu ZB, Liu J. Facile synthesis of yolk-shell Bi@C nanospheres with superior Li-ion storage performances. *Acta Metall Sin-Engl*. 2020;34: 347. <https://doi.org/10.1007/s40195-020-01117-w>.
- [32] Chen ZS, Wu YJ, Liu X, Zhang YW, Yang LC, Li HY. Bi/Bi₃Se₄ nanoparticles embedded in hollow porous carbon nanorod: high rate capability material for potassium-ion batteries. *J Energy Chem*. 2023;81:462. <https://doi.org/10.1016/j.jechem.2023.02.050>.
- [33] Devina W, Sarofil ADM, Chandra C, Park HS, Park JH, Chung KY, Chang W, Kim J. Reversible conversion-alloying of cobalt-bismuth oxide nanoneedles for long-life lithium storage anodes. *Appl Surf Sci*. 2023;623: -157013. <https://doi.org/10.1016/j.apsusc.2023.157013>.
- [34] Liu X, Sun ZF, Sun YJ, Lin HX, Chen ZS, Chen XX, Niu L, Zhang QB, Li HY. Fast and long-lasting potassium-ion storage enabled by rationally engineering strain-relaxation Bi/Bi₂O₃ nanodots embedded in carbon sheets. *Adv Funct Mater*. 2023; 52:2307205. <https://doi.org/10.1002/adfm.202307205>.
- [35] Kang WW, Sun Y, Xu B, Li J, Kong XD, Huang DF, Zhang XQ, Yang H, Lin BP. Novel aqueous nickel-bismuth batteries using NiMoO₄@NiCo-layered double hydroxide heterostructure nanoarrays and Bi₂O₂CO₃ microspheres as advanced electrode materials. *Electrochim Acta*. 2019;323: -134819. <https://doi.org/10.1016/j.electacta.2019.134819>.
- [36] Prajapati KA, Bhatnagar A. A review on anode materials for lithium/sodium-ion batteries. *J Energy Chem*. 2023;83:509. <https://doi.org/10.1016/j.jechem.2023.04.043>.
- [37] Pu FZ, Bai YL, Lv J, Zhao XT, Wu GC, Kong CC, Lei BS, Zhang XJ, Jin H, Yang ZM. Yolk-shell Cu₂O@CuO-decorated rGO for high-performance lithium-ion battery anode. *Energy Environ Mater*. 2021;5:253. <https://doi.org/10.1002/eem2.12160>.
- [38] Liu LM, Huang XX, Wei ZY, Duan XM, Zhong B, Xia L, Zhang T, Wang HT, Jia DC, Zhou Y, Zhang R. Solvents adjusted pure phase CoCO₃ as anodes for high cycle stability. *J Adv Ceram*. 2021;10:509. <https://doi.org/10.1007/s40145-020-0453-y>.
- [39] Lei Y, Li S, Du M, Mi J, Gao DC, Hao L, Jiang LJ, Luo M, Jiang WQ, Li F, Wang SH. Preparation of double-shell Si@SnO₂@C nanocomposite as anode for lithium-ion batteries by hydrothermal method. *Rare Met*. 2023;42 (9):2972. <https://doi.org/10.1007/s12598-023-02325-w>.
- [40] Zhao Y, Liu WX, Shao W, Li L, Zuo M, Hu J, Zhu JF, Wang H, Zhang XD. Elemental doping inhibits surface-state-mediated charge carrier trapping for promoting photocatalytic selective oxidation. *J Mater Chem A*. 2023;11:3594. <https://doi.org/10.1039/d2ta09702h>.
- [41] Zuo HR, Wu CY, Du HY, Guo ZY, Cheng YN, Yan QS. Interfacial coupling of 3D nanoflower-like Bi₂O₂CO₃ with PANI for tetracycline photocatalytic degradation and intermediate toxicity analysis. *Appl Surf Sci*. 2023;633: -157600. <https://doi.org/10.1016/j.apsusc.2023.157600>.
- [42] Wang B, Wang JY, Zhang Y, Mei Y, Lian PC. Electrochemical performance of Bi₂O₂CO₃ nanosheets as negative electrode material for supercapacitors. *Ceram Int*. 2017;43:9310. <https://doi.org/10.1016/j.ceramint.2017.04.092>.
- [43] Zhang PP, Zhai XH, Huang H, Zhou JF, Li XB, He YP, Guo ZC. Synergistic Na⁺ and F⁻ co-doping modification strategy to improve the electrochemical performance of Li-rich Li_{1.20}Mn_{0.54}Ni_{0.13}Co_{0.13}O₂ cathode. *Ceram Int*. 2020;46:24723. <https://doi.org/10.1016/j.ceramint.2020.06.263>.
- [44] Min WL, Chen XH, Huang SH, Liao YL, Liang ZY, Lei Y, Xu JT. High performance lithium ion battery cathode based reduced holey graphene oxides from spent lithium ion batteries. *Carbon*. 2023;210: 118038. <https://doi.org/10.1016/j.carbon.2023.118038>.
- [45] Etacheri V, Hong CN, Tang J, Pol VG. Cobalt nanoparticles chemically bonded to porous carbon nanosheets: a stable high-capacity anode for fast-charging lithium-ion batteries. *ACS Appl Mater Interfaces*. 2018;10:4652. <https://doi.org/10.1021/acsami.7b15915>.
- [46] Jiang C, Gao MM, Zhang SY, Huang L, Yu ST, Song ZQ, Wu Q. Chitosan/graphene oxide hybrid hydrogel electrode with porous network boosting ultrahigh energy density flexible supercapacitor. *Int J Biol Macromol*. 2023;225:1437. <https://doi.org/10.1016/j.ijbiomac.2022.11.201>.
- [47] Yu M, Huang Y, Liu XD, Zhao XX, Fan WQ, She KH. In situ modification of MXene nanosheets with polyaniline nanorods for lightweight and broadband electromagnetic wave absorption. *Carbon*. 2023;208:311. <https://doi.org/10.1016/j.carbon.2023.03.066>.
- [48] Cen BQ, Li KX, Yang R. Expedient and effectual capacitive deionization performance by chitosan-based carbon with



- hierarchical porosity. *Desalination*. 2022;531: -115703. <https://doi.org/10.1016/j.desal.2022.115703>.
- [49] Zhang XS, Qiu XQ, Lin JX, Lin ZH, Sun SR, Yin J, Alshareef HN, Zhang WL. Structure and interface engineering of ultra-high-rate 3D bismuth anodes for sodium-ion batteries. *Small*. 2023;19:2302071. <https://doi.org/10.1002/smll.202302071>.
- [50] Zhang WJ, Wang YX, Guo XL, Liu YY, Zheng YM, Zhang M, Li RL, Peng ZB, Wang ZM, Zhang T. High performance Bi₂O₂CO₃/rGO electrode material for asymmetric solid-state supercapacitor application. *J Alloys Compd*. 2021;855: -157394. <https://doi.org/10.1016/j.jallcom.2020.157394>.
- [51] Wang MX, Li HJ, Cheng XQ, Tian SZ, Wang XM. Graphene-encapsulated nitrogen-doped carbon@Bi enables rapid, ultrahigh and durable sodium storage. *Batteries Supercaps*. 2023;6: e202300055. <https://doi.org/10.1002/batt.202300055>.
- [52] Lyu T, Luo FQ, Wang Z, Jiang FT, Geng SZ, Zhuang Y, Lin X, Chen JK, Wang DC, Bu LZ, Tao L, Liang LZ, Zheng ZF. Bifunctional lithiophilic carbon fibers with hierarchical structure for high-energy lithium metal batteries. *Chem Eng J*. 2023;466: 143357. <https://doi.org/10.1016/j.cej.2023.143357>.
- [53] Xu ZX, Xu LY, Xu ZX, Deng ZP, Wang XL. N, O-codoped carbon nanosheet array enabling stable lithium metal anode. *Adv Funct Mater*. 2021;31:2102354. <https://doi.org/10.1002/adfm.202102354>.
- [54] Kim MK, Kim MS, Park JH, Kim J, Ahn CY, Jin A, Mun J, Sung YE. Bi-MOF derived micro/meso-porous Bi@C nanoplates for high performance lithium-ion batteries. *Nanoscale*. 2020;12:15214. <https://doi.org/10.1039/d0nr03219k>.
- [55] Yang JH, Xian J, Liu QL, Sun YM, Li GQ. Bi nanoparticles in situ encapsulated by carbon film as high-performance anode materials for Li-ion batteries. *J Energy Chem*. 2022;69:524. <https://doi.org/10.1016/j.jechem.2022.01.026>.
- [56] Fu H, Shi CH, Nie JJ, Wang J, Yao SW. Bi₂O₃ nanospheres coated in electrospun carbon spheres derived Bi@C used as anode materials for lithium-ion batteries. *J Alloys Compd*. 2022; 918: -165666. <https://doi.org/10.1016/j.jallcom.2022.165666>.
- [57] Ou X, Xiong XH, Zheng FH, Yang CH, Lin ZH, Hu RZ, Jin C, Chen Y, Liu ML. In situ X-ray diffraction characterization of NbS₂ nanosheets as the anode material for sodium ion batteries. *J Power Sour*. 2016;325:410. <https://doi.org/10.1016/j.jpowsour.2016.06.055>.
- [58] Chen S, Du YB, Ma HP, Wang ZT, Fan S, Zhang WM, Yang HY. Unusual hybrid magnesium storage mechanism in a new type of Bi₂O₂CO₃ anode. *Nano Lett*. 2023;23:9788. <https://doi.org/10.1021/acs.nanolett.3c02465>.
- [59] Zhang N, Meng QQ, Wu HY, Hu X, Zhang MM, Zhou AB, Li YT, Huang YX, Li L, Wu F, Chen RJ. Co-MOF as stress-buffered architecture: an engineering for improving the performance of NiS/SnO₂ heterojunction in lithium storage. *Adv Energy Mater*. 2023;13:2300413. <https://doi.org/10.1002/aenm.202300413>.
- [60] Yu J, Zhao D, Ma CS, Feng L, Zhang YH, Zhang LF, Liu Y, Guo SW. Vapor-phase derived ultra-fine Bismuth nanoparticles embedded in carbon nanotube networks as anodes for sodium and potassium ion batteries. *J Colloid Interface Sci*. 2023;643: 409. <https://doi.org/10.1016/j.jcis.2023.04.039>.
- [61] Cui X, Chen JX, Sun ZF, Wang L, Peng QQ, Xiao BS, Zhao LG, Zheng H, Wang Y, Wang JB, Chen XF, Zhang QB, Chen SQ. A general route for encapsulating monodispersed transition metal phosphides into carbon multi-chambers toward high-efficient lithium-ion storage with underlying mechanism exploration. *Adv Funct Mater*. 2023;33:2212100. <https://doi.org/10.1002/adfm.202212100>.
- [62] Hasyim MR, Rajagopalan R. Prediction of discharge performances of pseudocapacitors using their impedance characteristics. *J Electrochem Soc*. 2020;167: -013536. <https://doi.org/10.1149/1945-7111/ab6722>.

Springer Nature or its licensor (e.g. a society or other partner) holds exclusive rights to this article under a publishing agreement with the author(s) or other rightsholder(s); author self-archiving of the accepted manuscript version of this article is solely governed by the terms of such publishing agreement and applicable law.